

A Memristive Neural Decoder for Cryogenic Fault-Tolerant Quantum Error Correction

Victor Yon,^{1, 2, 3, 4, *} Frédéric Marcotte,^{5, 2, 3, 4, *} Pierre-Antoine Mouny,^{1, 2, 3, 4} Gebremedhin A. Dagnew,⁵ Bohdan Kulchytskyi,⁵ Sophie Rochette,¹ Yann Beilliard,^{5, 2, 3, 4} Dominique Drouin,^{1, 2, 3, 4} and Pooya Ronagh^{1, 6, 7, 8, †}

¹*Irréversible Inc., Sherbrooke, Québec, Canada*

²*Institut Interdisciplinaire d'Innovation Technologique (3IT),
Université de Sherbrooke, Sherbrooke, Québec, Canada*

³*Laboratoire Nanotechnologies Nanosystèmes (LN2 - IRL 3463) – CNRS,
Université de Sherbrooke, Sherbrooke, Québec, Canada*

⁴*Institut quantique (IQ), Université de Sherbrooke, Sherbrooke, Québec, Canada*

⁵*1QB Information Technologies (1QBit), Vancouver, British Columbia, Canada*

⁶*Institute for Quantum Computing, University of Waterloo, Waterloo, Ontario, Canada*

⁷*Department of Physics & Astronomy, University of Waterloo, Waterloo, Ontario, Canada*

⁸*Perimeter Institute for Theoretical Physics, Waterloo, Ontario, Canada*

(Dated: November 1, 2024)

Neural decoders for quantum error correction (QEC) rely on neural networks to classify syndromes extracted from error correction codes and find appropriate recovery operators to protect logical information against errors. Its ability to adapt to hardware noise and long-term drifts make neural decoders a promising candidate for inclusion in a fault-tolerant quantum architecture. However, given their limited scalability, it is prudent that small-scale (local) neural decoders are treated as first stages of multi-stage decoding schemes for fault-tolerant quantum computers with millions of qubits. In this case, minimizing the decoding time to match the stabilization measurements frequency and a tight co-integration with the QPUs is highly desired. Cryogenic realizations of neural decoders can not only improve the performance of higher stage decoders, but they can minimize communication delays, and alleviate wiring bottlenecks. In this work, we design and analyze a neural decoder based on an in-memory computation (IMC) architecture, where crossbar arrays of resistive memory devices are employed to both store the synaptic weights of the neural decoder and perform analog matrix–vector multiplications. In simulations supported by experimental measurements, we investigate the impact of TiO_x-based memristive devices' non-idealities on decoding fidelity. We develop hardware-aware re-training methods to mitigate the fidelity loss, restoring the ideal decoder's pseudo-threshold for the distance-3 surface code. This work provides a pathway to scalable, fast, and low-power cryogenic IMC hardware for integrated fault-tolerant QEC.

INTRODUCTION

Fault-tolerant quantum computation (FTQC) holds the promise of solving extremely difficult problems with efficient time and space complexity [1, 2]. However, this efficiency is at the cost of resource-intensive classical procedures that are required for protecting the logical quantum state of the quantum processor against noise [3]. This includes, (a) physically protecting the quantum state by cooling and isolating the quantum processor, and (b) performing quantum control and quantum error correction protocols. The former is the reason many quantum technologies operate at cryogenic temperatures. But, the latter requires classical computing circuits that have historically been designed and manufactured to operate at room temperature and their high heat dissipation hinders their use inside cryostats.

The transfer and processing of the data generated by quantum error correction (QEC) protocols present numerous challenges: (i) With the anticipated tens of mil-

lions of physical qubits needed for FTQC, the repeated microsecond-long error correction cycles would produce terabytes of syndrome data per second to be processed for days- or even months-long computations [2, 4, 5]. Transferring this amount of data from the cryogenic environment to classical electronics located at room temperature quickly leads to wiring bottlenecks [6]. (ii) Transferring small signals from measurement at the quantum processor level through multiple temperature stages to be processed by room temperature instrumentation requires careful amplification to mitigate the increased thermal noise at each stage. Finally, (iii), an FTQC implementation of non-Clifford gates requires active error correction, that is, real-time processing of the syndrome data by a decoder module, and application of the resulting recovery operations at a time scale comparable to the coherence time of the quantum system [7, 8]. Classical processors capable of operating accurately at cryogenic temperatures can mitigate these challenges. This requires computing with extremely low heat dissipation, as the cooling power of dilution refrigerators is limited (1 to 2 W at the 4 K stage).

Since single-flux quantum (SFQ) digital electronics are natively compatible with cryogenic temperatures, recent works [9–11] propose SFQ-based architectures for de-

* These authors contributed equally to this work.

† Corresponding author: pooya@irreversible.tech

coding using various heuristic approximations to graph-matching algorithms [12–14], while [11] proposes a binarized SFQ-based neural decoders. Those systems are highly complex and consume a lot of energy, casting doubts on the ability to fabricate them reliably and on their potential benefits. The main challenge in building scalable cryogenic fault-tolerant decoders is the need for high-density cryogenic memory blocks for storing at least two types of information:

- (a) The program data: Even the simplest decoding heuristics require complex computations that rely on large look-up tables to store the logic and execute the algorithmic steps of the decoder [15, 16].
- (b) The input data: Fault-tolerant error correction requires processing multiple rounds of imperfect stabilizer measurements (typically as a graph-based algorithm on a 3-dimensional lattice) at once. Moreover, current decoding logic depends on historical progression of the algorithm [17–19]. Therefore, some type of memory must store and recall a historical state of computation.

In this paper, we introduce a memristive neural decoder (MND) which combines the advantages of recurrent neural network (RNN) and the low-power consumption of resistive memory arrays to eliminate the issues related to storage and recall for both types of memory blocks. In neural decoders, the program data (item (i) above) is the weights and biases of a neural network [20]. This information is stored in the conductance states of the resistive memory devices which are physically tuned, thereby providing a realization of in-memory computation (IMC) [21]. In addition, an RNN comprises an *internal state* which is a real-valued vector (or a higher-dimensional tensor) that encodes a latent representation of its prior inference (the h wires in Fig. 1). The RNN will therefore not need to receive the syndrome data of multiple rounds of error correction at once, and instead stream their processing one at a time as they get generated, while updating its internal state in each iteration (from h_i to h_{i+1} in Fig. 1).

More specifically, we investigate TiO_x -based analog resistive memory devices using TiN electrodes [22]. A crossbar arrangement of these memory cells enables the matrix-vector multiplication (MVM) operations at the heart of neural network algorithms to be performed natively by relying on Ohm’s law and Kirchoff’s circuit law, thus removing the time- and energy-intensive process of moving data from memory to processing units [23]. Such non-volatile memristive devices have small footprints [24–27], and benefit from complementary metal-oxide-semiconductor (CMOS)-compatible fabrication processes [22], data retention time of up to 10 years [28], and analog switching dynamics [29], making them promising candidates for efficient MVM in terms of processing time, energy dissipation, and scalability [30–32]. Furthermore, they operate very well at cryogenic

temperatures [33–35], are robust to temperature variations, and can be calibrated to adjust to long-term drifts in the input signal or environmental noise.

Moreover, the MND processes neural activations (the feature tensors propagating forward along the network) as inherently analog signals which are never converted to digital data in binary representation. This allows for a much better footprints compared to the alternative CMOS-based digital (binary) memory technologies such as static random access memory (SRAM) and resistive random access memory which were previously considered for low-power digital neural decoding [36, 37]. We note that the mixed-signal nature of MND makes it attractive for soft decoding [38] by directly interfacing the readout resonator and eliminating long and error-prone amplification and measurement of syndrome bits. Since it is difficult to scale neural decoders up for large surface code patches, we envision that such a tightly integrated decoder-QPU hybrid system may be augmented with further (more global) decoding stages such as large scale Union-Find or collision clustering decoders [39, 40].

Our early MND prototype is fabricated in CMOS 180 nm and demonstrates cryogenic compatibility down to 35 K [41]. It exhibits a decoding delay of 1 μs per stabilizer measurement round, which is similar to Collision Clustering decoders able to perform real-time QEC by demonstrating a 2×2 stability experiment [42]. Our decoder delay is currently bottlenecked by the pulse width used at cryogenic temperature and could be reduced to 200 ns with minimal CMOS design optimization. It is expected that our processing delay will not increase significantly with larger QEC codes as analog RNN allows for parallel computation. Additionally, the MND prototype consumes 3.4 mW at 35 K to perform the RNN computation and 10.9 mW for the auxiliary electronics used to interface with the memristors. It is anticipated that the distance-3 MND will consume ~ 50 mW for the RNN computation and roughly 120 mW for the memristor/CMOS interfacing electronics in CMOS 180 nm. The power consumption can be significantly reduced by using smaller CMOS nodes, e.g., 22 nm FDSOI exhibits power consumption up to 70 times smaller than CMOS 180 nm [43], yielding to a 2.5 mW power consumption per distance-3 MND.

However, non-idealities of memristor arrays are known to deteriorate neural networks (NNs)’ performance [44–48], our study is focused on the impact of key TiO_x -based devices’ non-idealities on the accuracy of MNDs. Stuck-at fault devices have the greatest impact on the decoder’s performance. Therefore, we propose and implement two techniques for mitigating their detrimental effect. The hardware-aware (HWA) method consists of improving NNs’ robustness by re-training it while taking into account typical hardware constraints. In contrast, the device-specific (DS) re-training method uses the exact location of stuck-at fault devices to specifically adapt to the imperfections of a given device. We show that the latter approach allows for high-fidelity decoding of the

distance-3 surface code.

Our paper is structured as follows. First, we provide a formal definition of the decoding problem using a distance-3 surface code, we describe the NN architecture of our decoder, and present the corresponding memristive decoder circuit. We then experimentally characterize key non-idealities of the TiO_x -based resistive memory devices (e.g., programming variability, stuck-at fault rate, retention time). We then assess the impact of these non-idealities in simulations, and demonstrate that the HWA and DS re-training methods recover most of the ideal neural decoder's fidelity. Finally, we discuss the engineering advantages of leveraging analog IMC hardware for QEC decoding, and provide some future perspectives.

PROBLEM STATEMENT

Decoding the Surface Code

In Fig. 1, the process of active error correction via stabilizer measurements and decoding is schematized. Here, successful error correction amounts to matching the decoder-proposed recovery operator (r_X, r_Z) with the logical error (ϵ_X, ϵ_Z) afflicting the logical state $|\psi\rangle_L$ encoded by the error correcting code. The performance of the decoder is dependent on its speed due to idling errors associated with the decoding delay. Therefore, minimizing the decoding time as much as possible is desirable.

We consider the distance-3 rotated surface code, which can be realized with 17 physical qubits [49–51]. As shown in Fig. 2(a), the qubits are arranged on a square lattice, comprising data qubits (circles filled in white) and ancilla, or syndrome, qubits (circles filled in black). Data and syndrome qubits differ only in terms of their function within the code, and they can be implemented using physical systems such as superconducting circuits, trapped ions, quantum dots, or topological qubits. Each qubit interacts with its neighbours in a specified manner. The order and mechanism of interaction is determined by the stabilizers being measured, as shown in Fig. 2(b) and (c) for the stabilizers $X_e X_f X_g X_h$ and $Z_a Z_b Z_c Z_d$, respectively.

Neural Decoder Architecture

We consider an RNN decoder module similar to the ones described in Refs. [20] and [52]. It may be difficult to train neural decoders for arbitrarily large topological codes; however, we note that the largest topological patch that must be actively decoded during FTQC depends on the largest entangling gate between a logical magic state and other logical qubits [53]. Additionally, neural decoders are great candidates for inclusion in distributed [54] and hierarchical decoding schemes [55] in order to create larger-scale decoding systems. We restrict our benchmarking to the X syndromes because the

performance would be the same for the Z syndromes. Supplementary Information Note S1 describes the model used to simulate the quantum circuit and obtain the syndromes datasets and labels for training the RNN decoder. The generated syndromes dataset [56] is used to train and test the RNN.

Our RNN architecture is illustrated in Fig. 3(b). It consists of a fully connected recurrent layer and a fully connected output evaluation layer. There are 4 input nodes for receiving the syndrome data of an error correction round and 32 internal state nodes to store the hidden state of the previous round via recurrent connections. Assuming similar error rates for physical gates and measurements, the distance-3 code requires three QEC cycles to be fault tolerant [20, 52, 57]. The outputs of the recurrent layer, after application of the activation function, a rectified linear unit (ReLU) function in this case, are fed back to the input of the internal state nodes when the next error correction round's syndrome data (s^X) arrive to the input nodes, and the process is repeated for a total of at least 3 cycles, as illustrated in Fig. 3(a). In order to evaluate the logical error rate of the scheme, we measure the data qubits in the final cycle (see Supplementary Information Note S1).

After the fourth round has been provided to the input nodes, the output of the recurrent layer is forwarded to the output layer and passed through a threshold function. Subsequently, the neural decoder outputs a single binary result, 0 or 1, indicating whether a logical error has occurred at the end of the QEC rounds (see Fig. 3(d)).

Memristive Neural Decoder

We present a memristive electronic circuit to implement the neural decoder architecture discussed above, where the parameters of the neural network are stored in crossbar arrays of TiO_x resistive memory. The MND architecture is shown in Fig. 3(c). It comprises two distinct memristor arrays: the recurrent array, which maps the weights corresponding to the recurrent layer, and the output array, which maps the weights corresponding to the output layer [58], in accordance with the architecture shown in Fig. 3(b). Input ports receive data from syndrome measurements in the form of voltage pulses. Between the two crossbars of memristive devices, we perform an analog-to-digital conversion to apply a digital ReLU activation function. The output is then converted back into an analog signal in the form of a voltage pulse. Performing the activation function in the digital domain simplifies the circuit design by removing concerns about analog signal deterioration, as it offers full control over the shape of the signal sent into the second layer. The range and resolution of analog-to-digital converter (ADC) and digital-to-analog converter (DAC) is discussed in Supplementary Information Note S2. Finally, the output port provides the binary classification result of the decoder, which determines the recovery op-

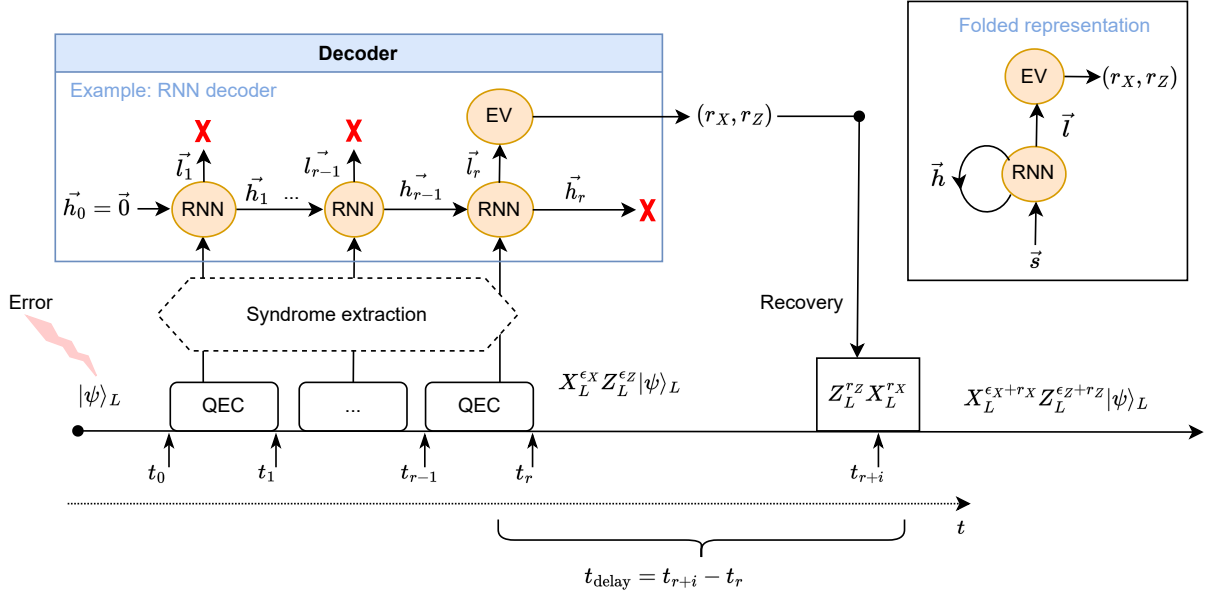


Figure 1. Decoding process. In quantum error correction (QEC), syndrome extraction rounds are performed cyclically to protect an encoded quantum state $|\psi\rangle_L$ from logical errors. Typically, the X and Z stabilizers' syndromes are processed separately but simultaneously by two independent decoding modules. The syndrome measurement outcomes are fed to the decoder modules, which analyze them to produce a decision output (r_X, r_Z) . This decision output is used to construct the recovery operation $Z_L^{r_Z} X_L^{r_X}$. Between the end of the last QEC round at t_r and the application of the recovery operation at t_{r+i} , idling errors can affect the qubits, and they will not be taken into account by the decoding algorithm. The encoded state just prior to the application of recovery operations is therefore $X_L^{\epsilon_X} Z_L^{\epsilon_Z} |\psi\rangle_L$, where $\epsilon_{x,z}$ represents the cumulative effect of the errors that occur during the QEC rounds and the idling time t_{delay} . Following the application of the recovery operation (here assumed to be ideal for simplicity), the final encoded logical quantum state is $X_L^{\epsilon_X + r_X} Z_L^{\epsilon_Z + r_Z} |\psi\rangle_L$. Here, the example decoder is based on a recurrent neural network (RNN). Each new syndrome is used as the input to the RNN and the hidden state \vec{h}_i is passed to the subsequent recurrence. At the end of the QEC process, the output state \vec{l}_r is passed to an evaluation module evaluation module (EV) (the fully connected output layer in the case of an RNN) to provide the final binary output of the decoder. On the right-hand side of the figure, the standard folded representation of this RNN is illustrated. A more detailed schematic architecture of this RNN decoder is depicted in Fig. 3.

eration to be applied to the surface code.

The memristor crossbar arrays needed to perform analog MVM consist of two TiN electrodes separated by a TiO_x-based switching layer [22]. Following an initial non-reversible electroforming process, a conductive filament containing oxygen vacancies is created within the oxide layer [59], which can be subsequently at least partially dissolved and re-established through voltage pulses applied on the electrodes, leading to programmable, non-volatile conductance states for the memristive device [60].

It is therefore possible to map the weight matrix of a NN layer into the conductance states G_{jk}^\pm of the memristors inside a crossbar array. To implement both positive and negative weights, a differential pair of memristive devices is used (see Fig. 3(b)). The weight-to-conductance mapping procedure is given by

$$G_{jk}^\pm = |w_{jk}| \frac{G_{\text{HCS}} - G_{\text{LCS}}}{w_{\text{max}}} + G_{\text{LCS}}, \quad (1)$$

where w_{max} is the absolute maximum weight of a given layer, and G_{HCS} and G_{LCS} are the highest conductance states (HCSs) and lowest conductance states (LCSs), respectively. In other words, they are the maximum and

minimum values that can be programmed on TiO_x-based memristive devices. If $w_{jk} > 0$, G_{jk}^+ is programmed with respect to Eq. (1) and G_{jk}^- is set to G_{LCS} . If $w_{jk} < 0$, G_{jk}^- is programmed with respect to Eq. (1) and G_{jk}^+ is set to G_{LCS} . After the RNN training has completed, the weights can be mapped to conductance states.

A crossbar configuration allows memristive devices to realize MVM natively, by relying on Ohm's law and Kirchhoff's current law. In Fig. 3(c), the current output of each column in the crossbar array is the sum of the input rows' voltages multiplied by the effective conductance values of the differential pairs of memristors. From the circuit laws, we have

$$i_k = \sum_j (G_{jk}^+ - G_{jk}^-) v_j, \quad (2)$$

where i and v denote output current and input voltage, respectively. For each differential amplifier, the symbols “+” and “−” set in superscript form denote the polarity of the pins wired to the memristors. From Eq. (2), each column implements naturally the multiply-accumulate (MAC) operation [61].

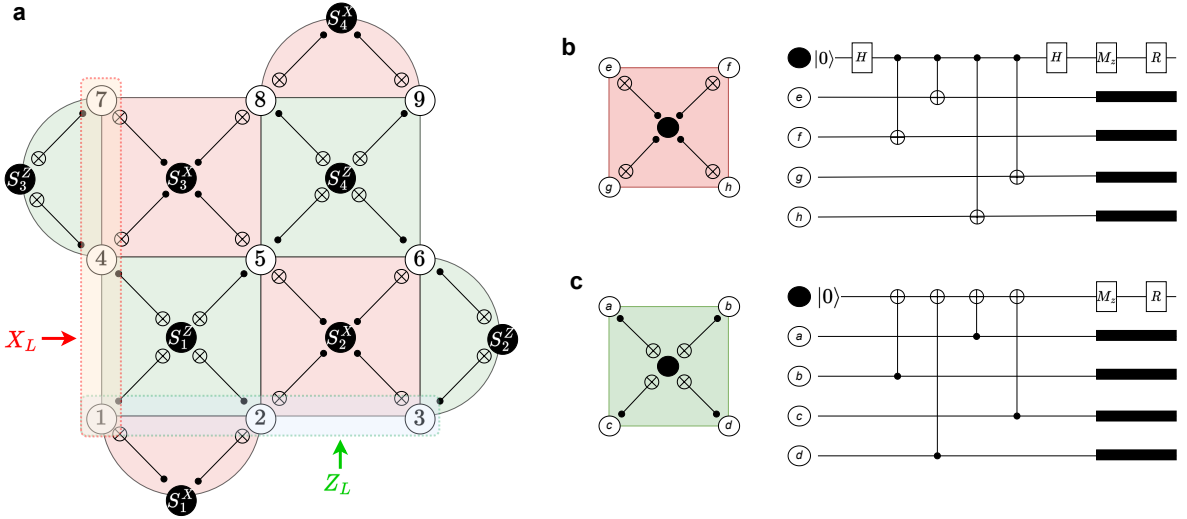


Figure 2. Surface code and stabilizer measurements. (a) Distance-3 rotated surface code, also called surface-17. Data qubits 1 to 9 are identified by circles filled in white, and syndrome qubits are identified by circles filled in black. Each syndrome qubit resides on a “plaquette” corresponding to a specific stabilizer measurement S . The sequence of operations realizing an X stabilizer (pink plaquette) and a Z stabilizer (green plaquette) are shown in (b) and (c). In this example, a logical operator X_L (Z_L) can be realized by applying a chain of physical X (Z) operators on data qubits between the top (left) and bottom (right) edge of the grid. (b) Sequence of circuit operations between a syndrome qubit (circle filled in black, the top qubit in the circuit) and its neighbouring data qubits, e , f , g , and h , realizing the stabilizer measurement $X_e X_f X_g X_h$. It consists of syndrome qubit initialization, Hadamard gates (H), CNOT gates, a projective measurement along the z -axis (M_Z), and a reset (R) to the $|0\rangle$ state, regardless of the measured outcome. (c) Sequence of circuit operations between a syndrome qubit and its neighbouring data qubits, a , b , c , and d , realizing the stabilizer measurement $Z_a Z_b Z_c Z_d$. It consists of syndrome qubit initialization, CNOT gates, a projective measurement along the z -axis (M_Z), and a reset (R) to the $|0\rangle$ state, regardless of the measured outcome. The black rectangles represent idling of the data qubits, which is important for simulation of the circuits. More details on the exact procedure used for the simulation of these parity-check circuits is provided in Supplementary Information Note S1.

ELECTRICAL CHARACTERIZATION

In this section, we describe and experimentally characterize various hardware non-idealities of TiO_x -based resistive memory devices. Due to the variability of the fabrication process and switching mechanisms, these devices exhibit multiple non-idealities [48, 62–64], such as read variability, programming variability, and stuck-at fault malfunction (that is, the memory devices become stuck in either HCS or LCS after electroforming or shortly after a conductance programming attempt [65]). These non-idealities are expected to decrease the fidelity of an MND. Other non-idealities such as random telegraphic noise and $1/f$ noise are also commonly reported for oxide-based devices [48]; however, we do not investigate their impact, as it is expected to be insignificant for high-speed MNDs operating with input voltage pulses in the nanosecond range. Regarding conductance state retention, Supplementary Information Fig. S3 shows no noticeable change in the conductance state after 8 hours, confirming the stability of the memory state of these devices, acceptable for target applications. Furthermore, we have recently demonstrated data retention at 4.2 K for over 15 minutes [34], suggesting that TiO_x -based resistive memory devices are good candidates for a cryogenic

MND.

Programming variability, also called cycle-to-cycle variability, is responsible for the inaccurate mapping of trained weights to the conductance states of memristors. Figure 4(a) shows the programming procedure of 11 conductance states on our fabricated memristors using a closed-loop read–write–verify algorithm [60] (see Supplementary Information Note S3). It can be seen that the target values given by Eq. (1) cannot be reached exactly due to the stochastic nature of the resistive switching process. Therefore, a programming variability model that accounts for cycle-to-cycle variability and device-to-device variability has been obtained from experimental characterizations of TiO_x -based resistive memory devices [34]. The characterization process is detailed in Supplementary Information Note S3. In this model, the actual programmed conductance values are expressed as

$$G_{jk}^{\pm} \leftarrow G_{jk}^{\pm} + \mathcal{N}(0, \sigma_{\text{prog}}(G_{jk}^{\pm})), \quad (3)$$

where $\sigma_{\text{prog}}(G_{jk}^{\pm})$ follows the polynomial fit of Fig. 4(b). The median value of the relative variations, that is, $\sigma_{\text{prog}}(G_{jk}^{\pm})/G_{jk}^{\pm}$, is 0.8 % for TiO_x -based resistive memory devices in the conductance range of [60, 200] μS .

The device yield of a chip is usually slightly under 100 % due to variations and imperfections in the nanofab-

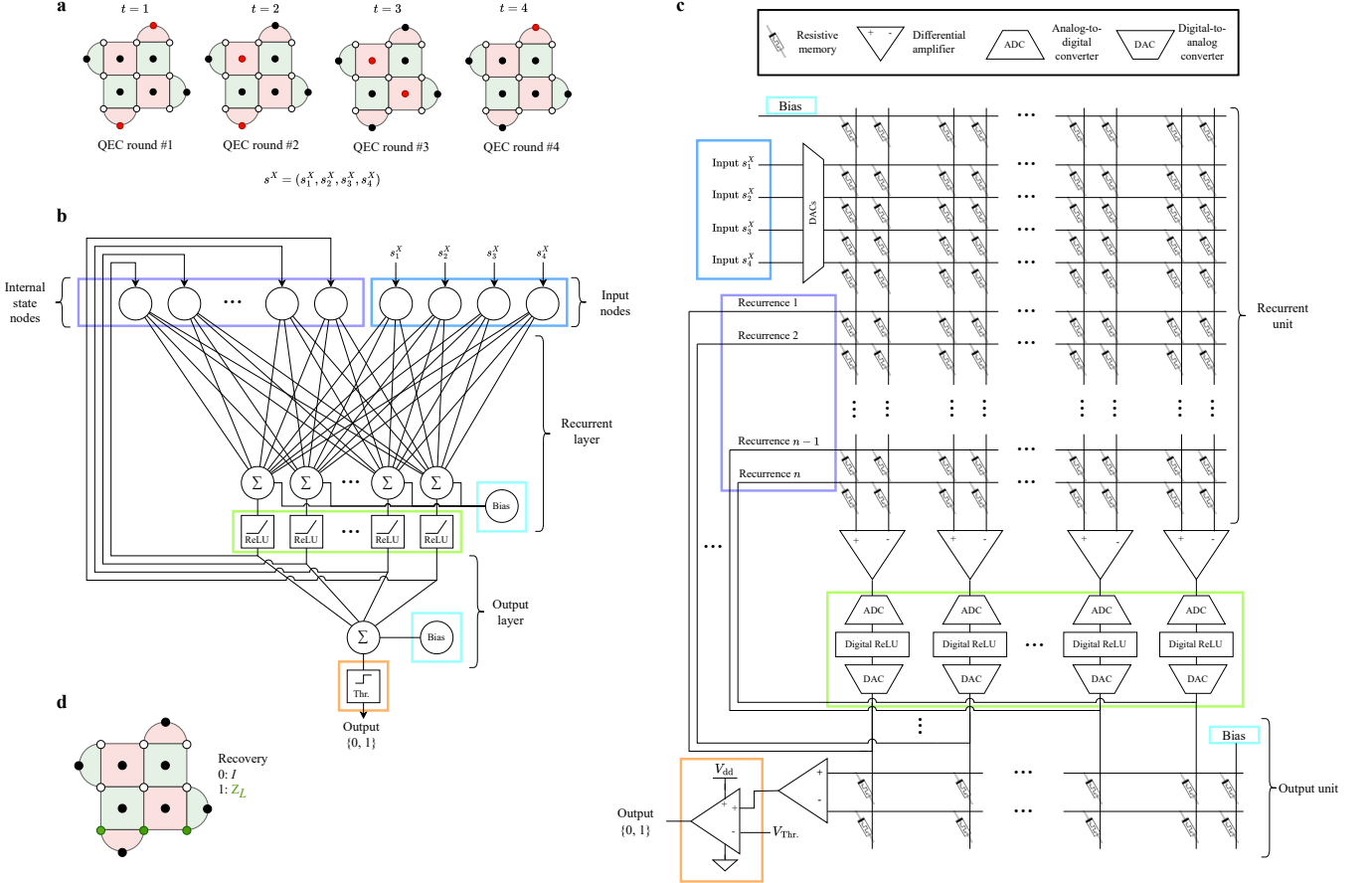


Figure 3. Recurrent neural network decoder architecture and corresponding memristive decoder circuit. Quantum error correction (QEC) is handled as a sequential classification problem. (a) Error correction rounds performed by measuring stabilizer operators on the lattice of physical qubits. Ancilla qubits (the circles filled in red or black representing an error or no error being detected, respectively) measure the bit-flip X (phase-flip Z) stabilizers \hat{S}_{1-4}^X (\hat{S}_{1-4}^Z). Measured eigenvalues of ancillas are mapped to classical bits to build the syndromes s^X and s^Z , which serve as inputs to the neural decoder. Here, we consider only the s^X syndromes, obtained at times $t = 1, 2, 3, 4$. (b) Recurrent neural network decoder architecture for the distance-3 surface code. It comprises a recurrent layer and an output layer. Bias is also applied to both layers. The syndrome at $t = 1$ is the initial input along with the initialized hidden state \vec{h}_0 . The output of the recurrent layer is routed back to be used as new input to the internal state nodes, as a new syndrome ($t = 2$) is provided to the input nodes. This is repeated until the last QEC round at time $t = n$ (here, $n = 4$), when the output of the recurrent layer is forwarded to the output layer, where the value of the single output neuron is compared to a threshold value to produce a binary classification. (c) Memristive decoder circuit. It is composed of two arrays of memristors. The first is applied recursively (recurrent array) until $t = n$, and the second acts as the classifier (output array). Input syndromes are converted from the digital domain to the analog domain by digital-to-analog converters so that the memristive crossbar can perform the analog matrix-vector multiplication. The memristor conductances are programmed according to the digitally trained weights of the equivalent neural network decoder. Differential amplifiers subtract the outputs from each pair of memristor columns to obtain the resulting node's value. This signal is forwarded to the activation function array (green rectangle), where an analog-to-digital conversion is performed to apply a digital ReLU activation function. The signal is converted back to the analog domain before being routed back to the recurrence input ports or sent to the output array. Finally, the value of the output array is passed through a comparator to produce a binary classification. An additional memristor row in each array allows the application of a bias signal. (d) Recovery operation. To conclude the QEC process, a recovery operation is applied to the data qubits according to the classification provided by the decoder. The identity is applied in the case where no logical error has been detected (output 0), and the Z_L operator is applied (circles filled in green) if a logical error has been detected (output 1).

rication process. This translates to a non-zero probability of stuck-at fault devices. In this case, the device cannot be programmed to the desired conductance for mapping a given weight of the NN. Recent work on passive cross-bars of memristors has shown a probability of stuck-at fault devices on the order of $\sim 1\%$ [66–68]. In the case of our TiO_x -based resistive memory devices, this probability can reach $\sim 10\%$ and the devices are usually stuck in their HCS.

RESULTS

Due to the hardware non-idealities characterized in the previous section, it is expected that the transfer of a digitally trained neural decoder to the equivalent memristor-based implementation would decrease its performance. We simulate the impact of these key non-idealities on the fidelity of an MND implemented in a mixed-signal IMC architecture. We then benchmark mitigation strategies using re-training allowing for almost complete compensation for the negative impact of the non-idealities of memristors.

We first evaluate the impact of the programming variability observed in TiO_x -based memristive devices by investigating their effects on the decoder performance. Figure 4(c) shows the evolution of the decoding fidelity of a distance-3 RNN for a typical physical fault rate of 10^{-2} when the programming noise is increased. The experiment is repeated 10 times to obtain a mean fidelity value (shown using a blue curve). Note that no noticeable fidelity decrease is observed below about 10 times the experimental noise value, therefore, the programming variability of TiO_x -based resistive memory devices does not represent a roadblock for the realization of the MND. Evaluating the impact of the resolution of the DACs and ADCs (see Supplementary Information Fig. S1) leads to the same conclusion, as an 8-bit discretization of the input and output values does not present any significant impact on the performance of the decoding. Lastly, the neural decoder appears to be robust against the reading variability (up to 1%) induced by the analog electronics during a MVM operation (see Fig. S2). The methodology used to evaluate the impact of the DACs and ADCs, and the reading variability is described in Supplementary Information Note S2.

We then study the impact of stuck-at fault devices on the fidelity of the neural decoder, which is expected to reach up to 10% for the evaluated memristor technology. To emulate the impact of this non-ideality, a random subset of network parameters is set to zero when testing the decoder. This situation corresponds to the case where one of the memristor of a differential pair is stuck in HCS or LCS and the other is either also stuck in the same state or purposefully programmed in order to bring the logical analog weight to zero. The results presented in Fig. 5(c) (green curve) show that, without any re-training designed to tackle this non-ideality, the

stuck-at fault rate significantly reduces the performance of the decoder. A decrease of more than 17% in fidelity is observed when the percentage of stuck-at fault devices during inference reaches 8% (this is equivalent to 15% of the model parameters, since a parameter is encoded via a pair of devices).

Therefore, we explore two re-training methods to attempt to restore the initial fidelity of the MND (see Fig. 5(a)), which we compare to two baselines:

- Digital baseline: an ideal version of the neural decoder that can perform syndrome processing at room temperature on classical hardware. The parameters are trained using a deep learning method [70] (see Supplementary Information Table S1) and are represented as 32-bit floating-point variables that do not include hardware non-idealities. The RNN architecture is based on Ref. [20]. The digital baseline performance is represented in black in Fig. 5, which we use as an upper bound and a reference against which to compare the other methods.
- MND baseline: a naïve implementation of an analog memristor-based neural decoder that could be integrated in a cryogenic environment. The RNN's architecture is identical to the digital baseline, but the parameters are converted into the equivalent memristor conductance values after digital training. Hardware constraints and memristor non-idealities are simulated based on experimental characterizations (see Supplementary Information Table S2), but no re-training is used. The MND baseline performance is represented in green in Fig. 5, which is expected to be a lower bound for other MND methods.
- Hardware-aware memristive neural decoder (HWA-MND): the MND baseline augmented with a re-training post-processing. The re-training consists of one additional training epoch during which different random weights are set to 0 at each forward pass. The dropconnect method [71] is typically used for regularization, but in the context of HWA re-training it is incorporated to improve the robustness of the RNN against stuck-at fault devices. For this reason, we set the dropconnect rate to match the expected number of weights blocked due to stuck-at fault devices in the characterized hardware (see Supplementary Information Fig. S4 for the different stuck-at fault rates). At the testing stage, the hardware non-idealities are simulated (see Supplementary Information Table S2). The performance of HWA-MND is represented in yellow in Fig. 5.
- Device-specific memristive neural decoder method (DS-MND): a variation of the HWA-MND, where the dropconnect is not random but follows a specific device. During the entire re-training epoch, the

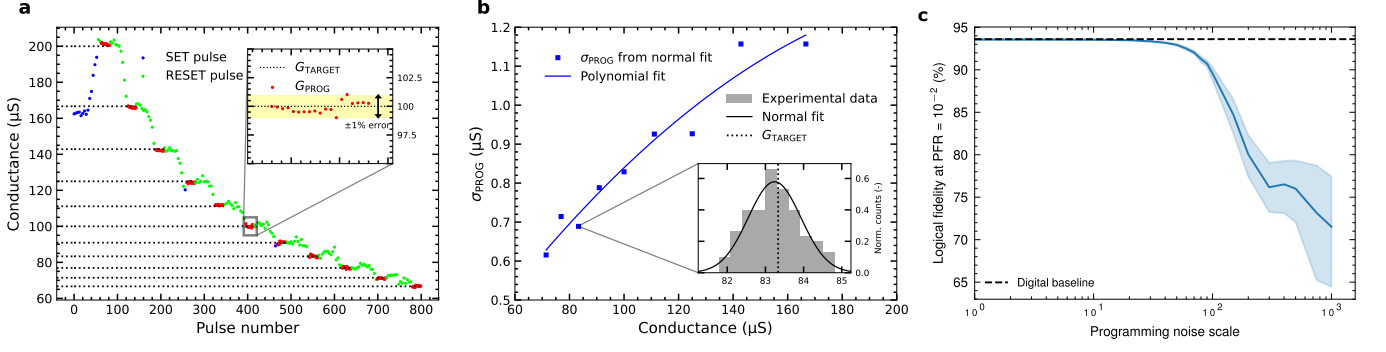


Figure 4. Programming variability characterizations of TiO_x -based resistive memory and its impact on the neural decoder. (a) Pulse programming of 11 conductance states of a TiO_x -based resistive memory device. Positive voltage pulses induce a conductance increase (labeled “SET pulse”) due to the growth of the conductive filament inside the TiO_x layer between the electrodes. Negative voltage pulses are employed to decrease the conductance (“RESET pulse”) due to the rupture of the conductive filament. The dotted black lines denote the target conductance (“ G_{TARGET} ”), whereas the red dots denote the programmed conductance (“ G_{PROG} ”) values upon convergence of the closed-loop read–write–verify algorithm. The inset is a zoom-in on the readout of the 100 μS state within the allowed error of 1 %. (b) Programming variability model based on the programming standard deviations of multiple conductance states. The multilevel programming cycle shown in (a) is conducted 10 times in a double sweep for 10 devices. For each conductance state, the standard deviation of the distribution of programmed values is extracted to fit a programming variability model, except for the highest conductance state (HCS) and the lowest conductance state (LCS). (c) Decoding fidelity of a distance-3 surface code for a typical physical fault rate of 10^{-2} using a trained recurrent neural network (RNN), as a function programming variability of the weights, represented as a factor of the polynomial fit used in (b). The error bands represent the 95 % confidence interval over 10 random seeds. The performance of the RNN remains close to the digital baseline before the noise standard deviation reaches a factor of ~ 10 times higher than the experimental value, after which the fidelity drops significantly.

weights corresponding to the stuck-at fault memristors in a given crossbar are fixed at 0. This approach forces the RNN to precisely adapt its parameters to this hardware limitation. The performance of DS-MND is represented in red in Fig. 5.

Supplementary Information Note S4 provides details about the implementation of training and inference in our experiments, and we have made the simulation data available in Ref. [72].

Dropping connections randomly during the HWA-MND re-training provides a generic mitigation strategy applicable to any crossbar of memristors given that the average number of stuck-at fault devices is known prior to re-training. However, it does not allow for a full recovery of the digital baseline performance even for low rates of stuck-at fault devices. DS-MND addresses this shortcoming. This re-training of DS-MND completely avoids updating weights that cannot be reliably programmed in the crossbar. The idea of this DS re-training is to leverage precise knowledge of the crossbars’ electrical characterizations to find the best NN parameters for that particular memristive circuit. It has the advantage of converging towards a nearly optimal solution, at the cost of having to individually characterize each crossbar of the MND to localize stuck-at fault devices, a task which can be performed through methods such as march tests [73, 74]. The simulation results, with the expected 10 % rate of stuck-at fault devices (see Fig. 5 (d)), show that only DS-MND reaches within 1 % of the digital baseline’s fidelity,

whereas the HWA-MND recovers only about half of the performance loss due to hardware non-idealities.

Fig. 5(b) represents the decoding performance of the MNDs studied in the case of different PFRs for a fixed percentage of stuck-at fault devices of 10 % to match the typical fabrication yield. Only the DS re-training method maintains the pseudo-threshold of the memristive decoder near the pseudo-threshold of the baseline decoder. Therefore, based on the characterized non-idealities of TiO_x -based resistive memory devices, it is a necessity to introduce specific knowledge of the chip during re-training to achieve the highest decoding performance in the case of a distance-3 code based on the RNN we have studied. The general solution provided by HWA-MND provides robustness against device-specific hardware issues, but remains insufficient.

DISCUSSION

In this section, we discuss our novel hardware approach for implementing an RNN decoder relying on the IMC paradigm to perform MVM on passive crossbars of memristors. We implemented a simulation based on the *IBM Analog Hardware Acceleration Kit* [69] that accounts for the experimentally characterized non-idealities of TiO_x -based resistive memory devices and measured their impact on our neural decoder’s performance. By applying computational methods to mitigate key hardware non-idealities, we improved the robustness of the neural

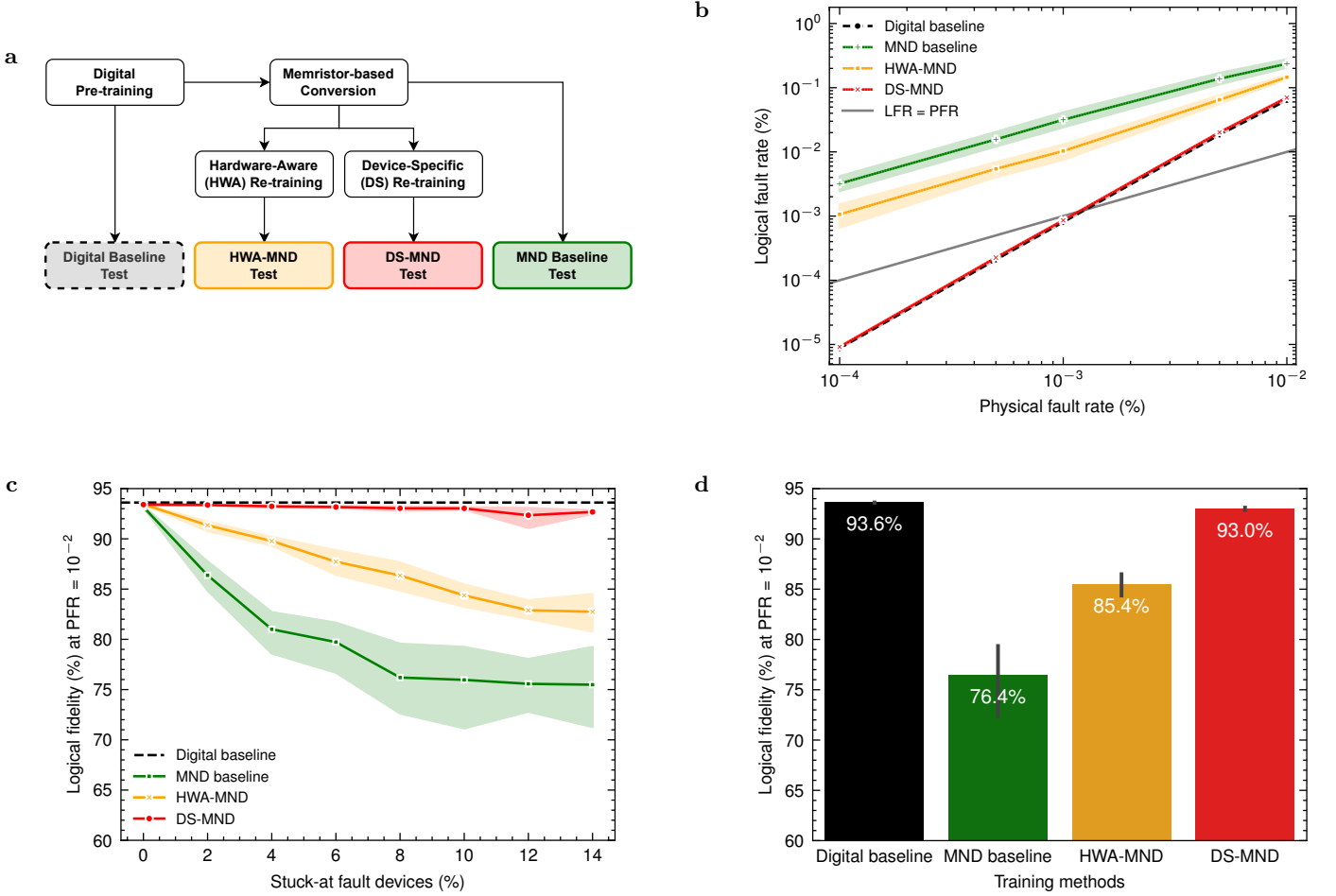


Figure 5. Baselines and re-training methods for the memristive neural decoder. (a) Schematic representation of the methods used to train the recurrent neural network (RNN) decoder. The fidelity of the digital baseline is tested immediately after classical training. The hardware-aware (HWA) and device-specific (DS) memristive neural decoder (MND) methods benefit from a re-training step after being converted to a memristor-based model with the *IBM Analog Hardware Acceleration Kit* [69], whereas the MND baseline training method is converted and tested without any re-training. (b) logical fault rate (LFR) after decoding as a function of the physical fault rate (PFR). The intersection between the line “LFR = physical fault rate (PFR)” and decoder performances represent the breakeven points (i.e., the pseudo-threshold values) of the corresponding neural decoders. (c) Logical fidelity percentage of the decoder at a PFR of 10^{-2} , for the baselines and the re-trained decoders, as a function of the percentage of stuck-at fault devices. For the HWA-MND, the stuck-at fault devices define the dropconnect rate used during re-training. (d) Logical fidelity percentage of the decoder at a PFR of 10^{-2} for the baselines and the re-trained decoders. For the results presented in (b) and (d), the rate of stuck-at fault devices is set at the expected fabrication yield of 10 %. For the results presented in (b), (c), and (d), the digital baseline fidelity is obtained with an equivalent neural decoder. The error bars and shaded regions represent the 95 % confidence interval over 10 random seeds.

decoder. In particular, we found that using the dropconnect method during re-training can greatly improve the fidelity of an MND that whose performance is significantly reduced by stuck-at fault devices. Moreover, we have seen that localizing stuck-at fault memory devices in the crossbars and using that knowledge to disable the corresponding connections during re-training can lead to a fidelity score comparable to that of the digital baseline (i.e., having a $<1\%$ difference). Furthermore, the MND exhibits only a small drop in the pseudo-threshold for the distance-3 surface code in numerical simulations (see

Fig. 5(b)). Therefore, we can conclude that our results support the effectiveness of specialized training methods for MNDs to achieve near-optimal performance.

Although an experimental proof of concept has not yet been performed on fully integrated hardware, the results we have presented offer a promising pathway to realizing high-fidelity neural decoders using IMC and analog memristive devices. One interesting avenue for future research is the development of a fully analog version of the memristive decoder circuit presented in this paper. Such an implementation would bring further benefits in

terms of the decoding time and energy efficiency. Analog activation functions have been reported in the literature [75]. For instance, the ReLU function can be applied in the analog domain using multimodal transistors [76]. It is therefore possible to envision MNDs using an analog activation function after the first layer instead of implementing an ADC followed by a digital activation function followed by a DAC, as presented in this paper. A practical circuit would also necessitate many more electronic components to realistically perform the decoding task, some of which we did not consider here. For example, transimpedance amplifiers (TIAs) would be needed to convert a current signal to a voltage signal at the output of each memristor row. Also, an analog memory unit might be necessary to store and transmit the hidden states' signals back to the recurrence input ports.

In our work, we made the assumption that imperfections arising from analog or digital CMOS components (e.g., noise introduced by differential amplifiers, TIAs, and ADCs/DACs; divergence of the analog activation function from its digital counterpart in the case of a fully analog implementation; and signal distortion arising from multiple recurrences) are much less critical in terms of the fidelity of the MND in comparison to the non-idealities exhibited by the memristors. However, future work should include a more exhaustive analysis of the impact of circuit-level imperfections (e.g., using training methodologies that have been introduced [77, 78]).

Scalability is a well-known issue for QEC decoders: as the error correction code distance increases, the syndrome space grows exponentially. Neural decoders thus require an exponentially larger dataset to learn about correlations between syndromes and the occurrences of logical errors. Our decoder cannot overcome the issue of scalability. However, it can be integrated in a multi-stage or hierarchical decoding scheme [54, 55, 79]. Multi-stage or hierarchical approaches have been proposed to improve the efficiency of NN-based decoders by using a combination of two decoding modules; in some instances [80], the first module is a simple classical decoder, and the second is a NN-based decoder. The role of the NN-based module is to act as a supervisor, identifying when the correction suggested by the simple decoder will lead to a logical error. This approach results in a constant execution time once the NN has been trained, regardless of the physical error rate, and scales linearly with the number of qubits in the code. A more recent study [81] demonstrates that NNs can be used as local decoders to remove an initial set of errors, thereby reducing the syndrome space and enabling the fast execution of a global decoder (minimum-weight perfect matching in the study) to correct the remaining errors. In this sense, a fully analog version of our MND could be integrated in a hierarchical decoding strategy and act as a local decoder to feed inputs to a global decoder.

Another challenge related to the scalability of decoders is the cryogenic compatibility of the chosen hardware. Indeed, as the number of physical qubits increases, to

avoid a wiring bottleneck between the control electronics at room temperature and the quantum processor in a cryogenic environment, it is highly beneficial to integrate the decoder hardware directly within the cryostat [6]. Within this scope, the energy consumption and thus the heat dissipation of the decoder should be minimized to avoid perturbations in the quantum system. The MND presented in this paper shows promise in terms of cryogenic compatibility as the MAC operations rely on an energy-efficient memristive IMC architecture instead of digital circuit blocks such as multipliers and adders. Even if current hardware implementations of NNs employing application-specific integrated circuits (ASICs) and field-programmable gate arrays (FPGAs) are not optimized in comparison to CPU-based approaches, they continue to suffer from the delays and energy expenditure associated with digital MAC operations. Furthermore, in recently proposed approaches introducing the idea of quantized IMC for QEC [36, 37], the implementations still require digital multipliers and adders. From their fast inference time and energy efficiency, MNDs are a promising technology for direct integration in a dilution refrigerator. However, the cryogenic compatibility of a memristor-based fully analog integrated circuit for QEC and the detailed characterization of its decoding time and power dissipation remains to be investigated.

CODE AND DATA AVAILABILITY

The code from our study is available from the corresponding author upon reasonable request. The syndromes dataset has been made publicly available [56] as well as the model training and simulation output data [72].

ACKNOWLEDGEMENTS

We thank our editor, Marko Bucyk, for his careful review and editing of the manuscript. The authors acknowledge the financial support received through the NSF's CIM Expeditions award (CCF-1918549). P. R. acknowledges the financial support of Mike and Ophelia Lazaridis, Innovation, Science and Economic Development Canada (ISED), and the Perimeter Institute for Theoretical Physics. Research at the Perimeter Institute is supported in part by the Government of Canada through ISED and by the Province of Ontario through the Ministry of Colleges and Universities. This work was supported by the Natural Sciences and Engineering Research Council of Canada (NSERC). LN2 is a French-Canadian joint International Research Laboratory (IRL-3463) funded and co-operated by the Centre National de la Recherche Scientifique (CNRS), the Université de Sherbrooke, the Université de Grenoble Alpes (UGA), the école Centrale de Lyon (ECL), and the Institut National des Sciences Appliquées de Lyon (INSA Lyon). It

is supported by the Fonds de Recherche du Québec – Nature et Technologie (FRQNT).

AUTHOR CONTRIBUTIONS

All authors contributed to this article and approved of the submitted version.

Victor Yon: methodology, software implementation, run simulations, results analysis and visualization, writing–original draft preparation.

Frédéric Marcotte: methodology, software implementation, run simulations, hardware characterization, writing–original draft preparation.

Pierre-Antoine Mouny: methodology, software implementation, hardware characterization, manuscript editing.

Gebremedhin A. Dagneu: methodology, syndrome dataset generation, manuscript editing.

Bohdan Kulchytskyy: syndrome dataset generation, manuscript review, supervision.

Sophie Rochette: methodology, manuscript editing, supervision.

Yann Beilliard: methodology, manuscript editing, supervision.

Dominique Drouin: manuscript review, supervision.

Pooya Ronagh: methodology, manuscript editing, supervision.

COMPETING INTERESTS

The authors declare no competing interests.

-
- [1] P. W. Shor, Algorithms for quantum computation: discrete logarithms and factoring, in *Proceedings 35th annual symposium on foundations of computer science* (Ieee, 1994) pp. 124–134.
 - [2] C. Gidney and M. Ekerå, How to factor 2048 bit RSA integers in 8 hours using 20 million noisy qubits, *Quantum* **5**, 433 (2021).
 - [3] J. Preskill, Reliable quantum computers, *Proceedings of the Royal Society of London. Series A: Mathematical, Physical and Engineering Sciences* **454**, 385 (1998).
 - [4] M. E. Beverland, P. Murali, M. Troyer, K. M. Svore, T. Hoefler, V. Kliuchnikov, G. H. Low, M. Soeken, A. Sundaram, and A. Vashchillo, Assessing requirements to scale to practical quantum advantage, arXiv preprint arXiv:2211.07629 (2022).
 - [5] D. Camps, E. Rrapaj, K. Klymko, B. Austin, and N. J. Wright, Evaluation of the classical hardware requirements for large-scale quantum computations, in *ISC High Performance 2024 Research Paper Proceedings (39th International Conference)* (Prometeus GmbH, 2024) pp. 1–12.
 - [6] D. J. Reilly, Challenges in scaling-up the control interface of a quantum computer, in *2019 IEEE International Electron Devices Meeting (IEDM)* (2019) pp. 31.7.1–31.7.6.
 - [7] J. Roffe, Quantum error correction: an introductory guide, *Contemporary Physics* **60**, 226 (2019).
 - [8] F. Battistel, C. Chamberland, K. Johar, R. W. J. Overwater, F. Sebastiano, L. Skoric, Y. Ueno, and M. Usman, Real-time decoding for fault-tolerant quantum computing: Progress, challenges and outlook (2023), 2303.00054.
 - [9] A. Holmes, M. R. Jokar, G. Pasandi, Y. Ding, M. Pedram, and F. T. Chong, NISQ+: Boosting quantum computing power by approximating quantum error correction, Preprint at <http://arxiv.org/abs/2004.04794> (2020).
 - [10] Y. Ueno, M. Kondo, M. Tanaka, Y. Suzuki, and Y. Tabuchi, QECool: On-Line Quantum Error Correction with a Superconducting Decoder for Surface Code, in *2021 58th ACM/IEEE Design Automation Conference (DAC)* (Ieee, 2021) pp. 451–456.
 - [11] Y. Ueno, M. Kondo, M. Tanaka, Y. Suzuki, and Y. Tabuchi, Qulatis: A quantum error correction methodology toward lattice surgery, in *2022 IEEE International Symposium on High-Performance Computer Architecture (HPCA)* (Ieee, 2022) pp. 274–287.
 - [12] N. Delfosse and N. H. Nickerson, Almost-linear time decoding algorithm for topological codes, *Quantum* **5**, 595 (2021).
 - [13] Y. Wu, N. Liyanage, and L. Zhong, An interpretation of Union-Find Decoder on Weighted Graphs (2022), 2211.03288.
 - [14] C. Chamberland, A. Kubica, T. J. Yoder, and G. Zhu, Triangular color codes on trivalent graphs with flag qubits, *New Journal of Physics* **22**, 023019 (2020).
 - [15] P. Das, C. A. Pattison, S. Manne, D. M. Carmean, K. M. Svore, M. Qureshi, and N. Delfosse, AFS: Accurate, Fast, and Scalable Error-Decoding for Fault-Tolerant Quantum Computers, in *2022 IEEE International Symposium on High-Performance Computer Architecture (HPCA)* (2022) pp. 259–273.
 - [16] N. Liyanage, Y. Wu, S. Tagare, and L. Zhong, Fpga-based distributed union-find decoder for surface codes, arXiv preprint arXiv:2406.08491 (2024).
 - [17] X. Tan, F. Zhang, R. Chao, Y. Shi, and J. Chen, Scalable surface-code decoders with parallelization in time, *PRX Quantum* **4**, 040344 (2023).
 - [18] L. Skoric, D. E. Browne, K. M. Barnes, N. I. Gillespie, and E. T. Campbell, Parallel window decoding enables scalable fault tolerant quantum computation, *Nature Communications* **14**, 7040 (2023).
 - [19] H. Bombín, C. Dawson, Y.-H. Liu, N. Nickerson, F. Pastawski, and S. Roberts, Modular decoding: parallelizable real-time decoding for quantum computers, arXiv preprint arXiv:2303.04846 (2023).
 - [20] C. Chamberland and P. Ronagh, Deep neural decoders for near term fault-tolerant experiments, *Quantum Science and Technology* **3**, 044002 (2018).
 - [21] N. Verma, H. Jia, H. Valavi, Y. Tang, M. Ozatay, L.-Y. Chen, B. Zhang, and P. Deaville, In-memory computing: Advances and prospects, *IEEE Solid-State Circuits Magazine* **11**, 43 (2019).
 - [22] A. El Mesoudy, G. Lamri, R. Dawant, J. Arias-Zapata, P. Gliech, Y. Beilliard, S. Ecoffey, A. Ruediger, F. Alibart, and D. Drouin, Fully CMOS-compatible passive TiO₂-based memristor crossbars for in-memory computing, *Microelectronic Engineering* **255**, 111706 (2022).
 - [23] K. Berggren, Q. Xia, K. K. Likharev, D. B. Strukov, H. Jiang, T. Mikolajick, D. Querlioz, M. Salinga, J. R. Erickson, S. Pi, *et al.*, Roadmap on emerging hardware and technology for machine learning, *Nanotechnology* **32**, 012002 (2020).
 - [24] L. Chua, Memristor-The missing circuit element, *IEEE Transactions on Circuit Theory* **18**, 507 (1971).
 - [25] D. B. Strukov, G. S. Snider, D. R. Stewart, and R. S. Williams, The missing memristor found, *Nature* **453**, 80 (2008).
 - [26] L. Chua, Resistance switching memories are memristors, *Applied Physics A* **102**, 765 (2011).
 - [27] M.-K. Song, J.-H. Kang, X. Zhang, W. Ji, A. Ascoli, I. Messaris, A. S. Demirkol, B. Dong, S. Aggarwal, W. Wan, S.-M. Hong, S. G. Cardwell, I. Boybat, J. sun Seo, J.-S. Lee, M. Lanza, H. Yeon, M. Onen, J. Li, B. Yildiz, J. A. del Alamo, S. Kim, S. Choi, G. Milano, C. Ricciardi, *et al.*, Recent advances and future prospects for memristive materials, devices, and systems, *ACS Nano* **17**, 11994 (2023).
 - [28] D. Kumar, R. Aluguri, U. Chand, and T. Tseng, Metal oxide resistive switching memory: Materials, properties and switching mechanisms, *Ceramics International* **43**, S547 (2017).
 - [29] J. Woo and S. Yu, Resistive memory-based analog synapse: The pursuit for linear and symmetric weight update, *IEEE Nanotechnology Magazine* **12**, 36 (2018).
 - [30] A. Sebastian, M. Le Gallo, R. Khaddam-Aljameh, and E. Eleftheriou, Memory devices and applications for in-memory computing, *Nature Nanotechnology* **15**, 529 (2020).
 - [31] A. Amirsoleimani, F. Alibart, V. Yon, J. Xu, M. R. Pazhouhandeh, S. Ecoffey, Y. Beilliard, R. Genov, and D. Drouin, In-Memory Vector-Matrix Multiplication in Monolithic Complementary

- Metal–Oxide–Semiconductor–Memristor Integrated Circuits: Design Choices, Challenges, and Perspectives, *Advanced Intelligent Systems* **2**, 2000115 (2020).
- [32] M. Hu, J. P. Strachan, Z. Li, E. M. Grafals, N. Davila, C. Graves, S. Lam, N. Ge, J. J. Yang, and R. S. Williams, Dot-product engine for neuromorphic computing: Programming 1T1M crossbar to accelerate matrix-vector multiplication, in *2016 53rd ACM/EDAC/IEEE Design Automation Conference (DAC)* (2016) pp. 1–6.
- [33] Y. Beiliard, F. Paquette, F. Brousseau, S. Ecoffey, F. Alibart, and D. Drouin, Conductive filament evolution dynamics revealed by cryogenic (1.5 K) multilevel switching of CMOS-compatible $\text{Al}_2\text{O}_3/\text{TiO}_2$ resistive memories, *Nanotechnology* **31**, 445205 (2020).
- [34] P.-A. Mouny, Y. Beiliard, S. Graveline, M.-A. Roux, A. E. Mesoudy, R. Dawant, P. Gliech, S. Ecoffey, F. Alibart, M. Pioro-Ladrière, and D. Drouin, Memristor-Based Cryogenic Programmable DC Sources for Scalable In Situ Quantum-Dot Control, *IEEE Transactions on Electron Devices* **70**, 1989 (2023).
- [35] P.-A. Mouny, R. Dawant, B. Galaup, S. Ecoffey, M. Pioro-Ladrière, Y. Beiliard, and D. Drouin, Analog programming of CMOS-compatible $\text{Al}_2\text{O}_3/\text{TiO}_{2-x}$ memristor at 4.2 K after metal-insulator transition suppression by cryogenic reforming, *Applied Physics Letters* **123**, 10.1063/5.0170058 (2023).
- [36] P. Wang, X. Peng, W. Chakraborty, A. I. Khan, S. Datta, and S. Yu, Cryogenic Benchmarks of Embedded Memory Technologies for Recurrent Neural Network based Quantum Error Correction, in *2020 IEEE International Electron Devices Meeting (IEDM)* (2020) pp. 38.5.1–38.5.4.
- [37] Y. Ichikawa, A. Goda, C. Matsui, and K. Takeuchi, Non-volatile Memory Application to Quantum Error Correction with Non-uniformly Quantized CiM, in *2022 IEEE International Memory Workshop (IMW)* (2022) pp. 1–4.
- [38] H. Ali, J. Marques, O. Crawford, J. Majaniemi, M. Serraperralta, D. Byfield, B. Varbanov, B. M. Terhal, L. DiCarlo, and E. T. Campbell, Reducing the error rate of a superconducting logical qubit using analog readout information, arXiv preprint arXiv:2403.00706 (2024).
- [39] N. Liyanage, Y. Wu, A. Deters, and L. Zhong, Scalable quantum error correction for surface codes using fpga (2023), 2301.08419.
- [40] B. Barber, K. M. Barnes, T. Bialas, O. Buğdaycı, E. T. Campbell, N. I. Gillespie, K. Johar, R. Rajan, A. W. Richardson, L. Skoric, C. Topal, M. L. Turner, and A. B. Ziad, A real-time, scalable, fast and highly resource efficient decoder for a quantum computer (2023), 2309.05558.
- [41] P.-A. Mouny, M. Benhouria, V. Yon, P. Dufour, L. Huang, Y. Beiliard, S. Rochette, D. Drouin, and P. Ronagh, Towards a Cryogenic CMOS-Memristor Neural Decoder for Quantum Error Correction, in *2024 IEEE International Conference on Quantum Computing and Engineering (QCE)* (2024).
- [42] L. Caune, L. Skoric, N. S. Blunt, A. Ruban, J. McDaniel, J. A. Valery, A. D. Patterson, A. V. Gramolin, J. Majaniemi, K. M. Barnes, T. Bialas, O. Buğdaycı, O. Crawford, G. P. Gehér, H. Krovi, E. Matekole, C. Topal, S. Polletto, M. Bryant, K. Snyder, N. I. Gillespie, G. Jones, K. Johar, E. T. Campbell, and A. D. Hill, *Demonstrating real-time and low-latency quantum error correction with superconducting qubits* (2024).
- [43] A. Stillmaker and B. Baas, Scaling equations for the accurate prediction of CMOS device performance from 180 nm to 7 nm, *Integration* **58**, 74–81 (2017).
- [44] V. Joshi, M. Le Gallo, S. Haefeli, I. Boybat, S. R. Nandakumar, C. Piveteau, M. Dazzi, B. Rajendran, A. Sebastian, and E. Eleftheriou, Accurate deep neural network inference using computational phase-change memory, *Nature Communications* **11**, 2473 (2020).
- [45] C. Wang, D. Feng, W. Tong, J. Liu, Z. Li, J. Chang, Y. Zhang, B. Wu, J. Xu, W. Zhao, Y. Li, and R. Ren, Cross-point resistive memory: Nonideal properties and solutions, *ACM Transactions on Design Automation of Electronic Systems* **24**, 1–37 (2019).
- [46] Y. Xi, B. Gao, J. Tang, A. Chen, M.-F. Chang, X. S. Hu, J. V. D. Spiegel, H. Qian, and H. Wu, In-memory learning with analog resistive switching memory: A review and perspective, *Proceedings of the IEEE* **109**, 14–42 (2021).
- [47] I. Chakraborty, M. Ali, A. Ankit, S. Jain, S. Roy, S. Sridharan, A. Agrawal, A. Raghunathan, and K. Roy, Resistive crossbars as approximate hardware building blocks for machine learning: Opportunities and challenges, *Proceedings of the IEEE* **108**, 2276–2310 (2020).
- [48] V. Yon, A. Amirsoleimani, F. Alibart, R. G. Melko, D. Drouin, and Y. Beiliard, Exploiting non-idealities of resistive switching memories for efficient machine learning, *Frontiers in Electronics* **3**, 10.3389/felec.2022.825077 (2022).
- [49] H. Bombin and M. A. Martin-Delgado, Optimal resources for topological two-dimensional stabilizer codes: Comparative study, *Phys. Rev. A* **76**, 012305 (2007).
- [50] C. Horsman, A. G. Fowler, S. Devitt, and R. Van Meter, Surface code quantum computing by lattice surgery, *New Journal of Physics* **14**, 123011 (2012).
- [51] Y. Tomita and K. M. Svore, Low-distance surface codes under realistic quantum noise, *Physical Review A* **90**, 062320 (2014).
- [52] P. Baireuther, T. E. O’Brien, B. Tarasinski, and C. W. J. Beenakker, Machine-learning-assisted correction of correlated qubit errors in a topological code, *Quantum* **2**, 48 (2018).
- [53] D. Litinski, A game of surface codes: Large-scale quantum computing with lattice surgery, *Quantum* **3**, 128 (2019).
- [54] S. Varsamopoulos, K. Bertels, and C. G. Almudever, Decoding surface code with a distributed neural network-based decoder, *Quantum Machine Intelligence* **2**, 3 (2020).
- [55] N. Delfosse, Hierarchical decoding to reduce hardware requirements for quantum computing (2020), 2001.11427.
- [56] V. Yon and G. Dagnew, A memristive neural decoder for cryogenic fault-tolerant quantum error correction - syndromes dataset, 10.5281/zenodo.11166209 (2024).
- [57] C. Chamberland and M. E. Beverland, Flag fault-tolerant error correction with arbitrary distance codes, *Quantum* **2**, 53 (2018).
- [58] T. Gokmen, M. J. Rasch, and W. Haensch, Training LSTM Networks With Resistive Cross-Point Devices, *Frontiers in Neuroscience* **12** (2018).
- [59] V. Milo, G. Malavena, C. Monzio Compagnoni, and D. Ielmini, Memristive and CMOS Devices for Neuromorphic Computing, *Materials* **13**, 166 (2020).
- [60] F. Alibart, L. Gao, B. D. Hoskins, and D. B. Strukov, High precision tuning of state for memristive devices by adaptable variation-tolerant algorithm, *Nanotechnology*

- 23**, 075201 (2012).
- [61] D. Ielmini and H.-S. P. Wong, In-memory computing with resistive switching devices, *Nature Electronics* **1**, 333 (2018).
 - [62] Y. Zhang, P. Huang, B. Gao, J. Kang, and H. Wu, Oxide-based filamentary RRAM for deep learning, *Journal of Physics D: Applied Physics* **54**, 083002 (2020).
 - [63] G. C. Adam, A. Khayat, and T. Prodromakis, Challenges hindering memristive neuromorphic hardware from going mainstream, *Nature Communications* **9**, 10.1038/s41467-018-07565-4 (2018).
 - [64] C. Wang, D. Feng, W. Tong, J. Liu, Z. Li, J. Chang, Y. Zhang, B. Wu, J. Xu, W. Zhao, Y. Li, and R. Ren, Cross-point resistive memory, *ACM Transactions on Design Automation of Electronic Systems* **24**, 1 (2019).
 - [65] C.-Y. Chen, H.-C. Shih, C.-W. Wu, C.-H. Lin, P.-F. Chiu, S.-S. Sheu, and F. T. Chen, Rram defect modeling and failure analysis based on march test and a novel squeeze-search scheme, *IEEE Transactions on Computers* **64**, 180 (2015).
 - [66] H. Kim, M. R. Mahmoodi, H. Nili, and D. B. Strukov, 4K-memristor analog-grade passive crossbar circuit, *Nature Communications* **12**, 10.1038/s41467-021-25455-0 (2021).
 - [67] J. Jang, S. Gi, I. Yeo, S. Choi, S. Jang, S. Ham, B. Lee, and G. Wang, A Learning-Rate Modulable and Reliable TiO_x Memristor Array for Robust, Fast, and Accurate Neuromorphic Computing, *Advanced Science* **9**, 2201117 (2022).
 - [68] H. Yeon, P. Lin, C. Choi, S. H. Tan, Y. Park, D. Lee, J. Lee, F. Xu, B. Gao, H. Wu, H. Qian, Y. Nie, S. Kim, and J. Kim, Alloying conducting channels for reliable neuromorphic computing, *Nature Nanotechnology* **15**, 574 (2020).
 - [69] M. J. Rasch, D. Moreda, T. Gokmen, M. Le Gallo, F. Carta, C. Goldberg, K. El Maghraoui, A. Sebastian, and V. Narayanan, A flexible and fast pytorch toolkit for simulating training and inference on analog crossbar arrays, in *2021 IEEE 3rd International Conference on Artificial Intelligence Circuits and Systems (AICAS)* (2021) pp. 1–4.
 - [70] Y. LeCun, Y. Bengio, and G. Hinton, Deep learning, *nature* **521**, 436 (2015).
 - [71] L. Wan, M. Zeiler, S. Zhang, Y. Le Cun, and R. Fergus, Regularization of neural networks using dropconnect, in *Proceedings of the 30th International Conference on Machine Learning*, Proceedings of Machine Learning Research, Vol. 28, edited by S. Dasgupta and D. McAllester (Pmlr, Atlanta, Georgia, USA, 2013) pp. 1058–1066.
 - [72] V. Yon, A memristive neural decoder for cryogenic fault-tolerant quantum error correction - simulation data, 10.5281/zenodo.11164068 (2024).
 - [73] A. van de Goor and Y. Zorian, Effective march algorithms for testing single-order addressed memories, in *1993 European Conference on Design Automation with the European Event in ASIC Design* (1993) pp. 499–505.
 - [74] Y.-X. Chen and J.-F. Li, Fault modeling and testing of 1T1R memristor memories, in *2015 IEEE 33rd VLSI Test Symposium (VTS)* (2015) pp. 1–6.
 - [75] O. Krestinskaya, B. Choubey, and A. P. James, Memristive GAN in Analog, *Scientific Reports* **10**, 10.1038/s41598-020-62676-7 (2020).
 - [76] I. Surekcigil Pesch, E. Bestelink, O. de Sagazan, A. Mehonic, and R. A. Sporea, Multimodal transistors as ReLU activation functions in physical neural network classifiers, *Scientific Reports* **12**, 10.1038/s41598-021-04614-9 (2022).
 - [77] B. Liu, H. Li, Y. Chen, X. Li, T. Huang, Q. Wu, and M. Barnell, Reduction and IR-drop compensations techniques for reliable neuromorphic computing systems, in *2014 IEEE/ACM International Conference on Computer-Aided Design (ICCAD)* (2014) pp. 63–70.
 - [78] B. Liu, H. Li, Y. Chen, X. Li, Q. Wu, and T. Huang, Vortex: Variation-aware training for memristor X-bar, in *2015 52nd ACM/EDAC/IEEE Design Automation Conference (DAC)* (2015) pp. 1–6.
 - [79] K. Meinerz, C.-Y. Park, and S. Trebst, Scalable neural decoder for topological surface codes, *Phys. Rev. Lett.* **128**, 080505 (2022).
 - [80] S. Varsamopoulos, K. Bertels, and C. G. Almudever, Comparing Neural Network Based Decoders for the Surface Code, *IEEE Transactions on Computers* **69**, 300 (2020).
 - [81] C. Chamberland, L. Goncalves, P. Sivarajah, E. Peterson, and S. Grimberg, Techniques for combining fast local decoders with global decoders under circuit-level noise, Preprint at <https://arxiv.org/abs/2208.01178> (2022).
 - [82] O. Higgott, Pymatching: A Python package for decoding quantum codes with minimum-weight perfect matching (2021), 2105.13082.
 - [83] M. Spear, J. E. Kim, C. H. Bennett, S. Agarwal, M. J. Marinella, and T. P. Xiao, The impact of analog-to-digital converter architecture and variability on analog neural network accuracy, *IEEE Journal on Exploratory Solid-State Computational Devices and Circuits* **9**, 176 (2023).
 - [84] C. Wang, H. Wu, B. Gao, T. Zhang, Y. Yang, and H. Qian, Conduction mechanisms, dynamics and stability in ReRAMs, *Microelectronic Engineering* **187-188**, 121 (2018).
 - [85] A. Paszke, S. Gross, F. Massa, A. Lerer, J. Bradbury, G. Chanan, T. Killeen, Z. Lin, N. Gimelshein, L. Antiga, A. Desmaison, A. Kopf, E. Yang, Z. DeVito, M. Raison, A. Tejani, S. Chilamkurthy, B. Steiner, L. Fang, J. Bai, and S. Chintala, Pytorch: An imperative style, high-performance deep learning library, in *Advances in Neural Information Processing Systems 32* (Curran Associates, Inc., 2019) pp. 8024–8035.
 - [86] D. P. Kingma and J. Ba, Adam: A method for stochastic optimization (2017), 1412.6980.

Supplementary Information: A Cryogenic Memristive Neural Decoder for Fault-Tolerant Quantum Error Correction

S1. SIMULATION OF QUANTUM STABILIZER CIRCUITS

Here we provide some background on the simulation of surface codes and the error model used to generate the dataset for the neural decoder's training and testing (the dataset is available for download [56]). Our experiment is based on the distance-3 rotated surface code. This surface code corresponds to a 17-qubit system in which there are 9 data qubits (circles filled in white in Fig. 2(a) of the main manuscript) and 8 ancilla qubits (circles filled in black) corresponding to the 8 stabilizer generators $S_1^X, S_2^X, S_3^X, S_4^X, S_1^Z, S_2^Z, S_3^Z$, and S_4^Z .

In our study, we rely on Stim [2] to generate the circuits shown in Fig. 2 required to simulate the rotated surface code, PyMatching [82] for decoding with minimum-weight perfect matching in order to benchmark the relative performance of the recurrent neural network (RNN) decoder, and a custom-built glue code to integrate Stim and PyMatching. While writing this paper, the need for the glue code was eliminated due to recent updates in PyMatching2.

We simulate the memory- X rotated surface code, where preparation and final measurements are done in the X -basis. In addition, we conduct this simulation under circuit level noise, which means the following:

- with a noise probability of p , each two-qubit gate is followed by a two-qubit Pauli error drawn uniformly and independently from $\{I, X, Y, Z\}^{\otimes 2} \setminus \{I \otimes I\}$;
- with a probability of $2p/3$, the preparation of the $|0\rangle$ state is replaced by the state $|1\rangle = X|0\rangle$. Similarly, with a probability of $2p/3$, the preparation of the $|+\rangle$ state is replaced by the state $|-\rangle = Z|+\rangle$;
- with a probability of $2p/3$, any single-qubit measurement has its outcome flipped; and
- with a probability of p , each idling-qubit location is followed by a Pauli error drawn uniformly and independently from the stabilizer set $\{X, Y, Z\}$.

A Stim circuit is first initialized with a probability p for a given code distance and a number of rounds. This circuit is then repeatedly called to generate samples. The steps taken during circuit generation for performing the parity-check rounds shown in Fig. 2(b) and (c) of the main manuscript are detailed as follows:

1. At the onset of the quantum error correction (QEC) cycle, the data qubits are initialized in the $|+\rangle$ state (for memory- X experiments), while ancilla qubits are set to the $|0\rangle$ state. These are replaced with the states $|+\rangle$ and $|1\rangle$, respectively, with a probability of $2p/3$, accounting for preparation errors.
2. Before the beginning of every parity check round, each data qubit is depolarized with a probability of p due to idling.
3. To perform the parity-check circuits depicted in Fig. 2(b) and (c), Hadamard gates are applied to the X -syndrome qubits, converting the $|0\rangle$ states to $|+\rangle$ states and the $|1\rangle$ states to $|-\rangle$ states, followed by single-qubit depolarizing noise with a probability of p .
4. Next, four CNOT cycles are executed, and each cycle is succeeded by two-qubit depolarizing noise with a probability of p , following the configuration outlined in Fig. 2(b) and (c).
5. Hadamard gates are applied to the X -syndrome ancilla qubits, followed by depolarizing noise with a probability of p .
6. With a measurement error probability of $2p/3$, all ancilla qubits are measured in the Z -basis, after which they are reset to the $|0\rangle$ state.
7. To simulate preparation errors for the next QEC round, bit flips are applied with a probability of $2p/3$ on the ancilla qubits, along with idling, and steps 2 to 7 are repeated to conduct repeated syndrome measurement cycles.
8. Finally, the data qubits are measured in the X -basis with a measurement error a probability of $2p/3$. The data qubit measured implicitly define one final round of computational-basis-type stabilizers (in this case X stabilizers) inferred via the corresponding parity-check matrix. Since this is a classical process and is not subject to the circuit-level noise defined during a typical stabilizer round, the syndromes extracted in this round are also referred to as "perfect syndromes". The final state of the encoded logical qubit is then determined.

The first stabilizer measurement round is the encoding round, which creates an entangled logical qubit. In the absence of an error, the encoding results in a logical $|+\rangle$ state since the data qubits are initialized in a logical $|+\rangle$ state. Measuring a $|-\rangle$ logical state in the end thus indicates a logical error, and the goal of a decoder is to predict such events.

To generate samples for training the RNN, we first separate the X and Z syndromes, focusing only on the X syndromes. Next, we divide the X -syndrome measurements into separate time steps, corresponding to each syndrome extraction round. The training label represents the logical bit-flip value, where 0 indicates that the logical state corresponding to the given syndromes has remained unchanged, and 1 indicates that the logical state has flipped. The training, validation, and testing samples are generated using noise probabilities between $p = 0.00001$ and $p = 0.01$, along with 3 rounds of stabilizer measurement and then a reset.

A key preprocessing step before feeding measurements to the decoder for analysis is to take the differences between consecutive measurement outcomes. Syndromes indicate the presence or absence, as well as the type, of errors that have occurred to the physical qubits. The RNN outputs a prediction of 0 or 1, representing the absence or presence of a logical error, respectively. The corresponding recovery operator is thus given by $(Z_L)^y$, where y is the binary output of the RNN.

S2. OTHER HARDWARE NON-IDEALITIES

Analog-to-Digital and Digital-to-Analog Converter Range and Resolution

To simulate the behaviour of analog-to-digital converters (ADCs) and digital-to-analog converters (DACs) during inference on the crossbar arrays of memristors, a rounding function is applied,

$$f(x) = \begin{cases} -b & x < -b \\ \text{round}\left(\frac{x}{\frac{2b}{n}}\right) \frac{2b}{n} & -b \leq x \leq b \\ b & x > b \end{cases}, \quad (\text{S1})$$

where x represents the ADC and DAC input, its range is given by $[-b, b]$, and n is the number of quantization steps, for example, 256 for 8-bit resolution. The round function rounds the floating-point value to the closest integer. Based on the typical matrix-vector multiplication (MVM) output values, we fix the ADC range to $b = 6$. The DAC range is fixed to $b = 1$ to match with the sigmoid output range. In ADCs and DACs, there is a trade-off between resolution and acquisition frequency, that is, a lower resolution yields a higher acquisition frequency. An application where inference time needs to be minimized, such as with the neural decoder, requires a high acquisition frequency. From Fig. S1, we can see that an 8-bit resolution is appropriate to reach the highest acquisition frequency without substantially degrading the RNN decoder's fidelity. Therefore, we simulate ADC and DAC discretization during the testing of a memristive neural decoder (memristive neural decoder (MND)), but no re-training strategy seems necessary to maintain the decoder's fidelity.

Reading Variability

Every analog electronic component induces a small reading variability. Analog-to-digital converters and digital-to-analog converters [83]; differential amplifiers; and memristors [84] involved in MVM operations are no exception. Based on experimental characterizations [34], we estimate that the dominant source of reading variability should come from memristors. To reduce the computational complexity, we simplify the simulation by considering every source of reading variability as one Gaussian random value added at the output of each row of memristors. As a conservative estimate, we chose a Gaussian distribution with a standard deviation equal to 1% of the maximum logical value (defined as b in the previous section).

The effect of different reading noise on the neural decoder's fidelity is illustrated in Fig. S2. This simulation result suggests that a 1% reading noise is not detrimental to our decoding application. However the performance drops quickly when the value increases above this limit. We can observe that the random dropconnect applied with our hardware-aware memristive neural decoder (hardware-aware (HWA)-MND) re-training method also increases the robustness of the model against high reading variability. The device-specific memristive neural decoder (device-specific (DS)-MND) re-training method is more sensitive to perturbations that are not related to the stuck-at fault devices; this is visible by the faster fidelity drop in Fig. S2 when the output noise is increased in comparison to the HWA-MND method. This reading variability study shows that realistic noise values do not impact the performance enough to

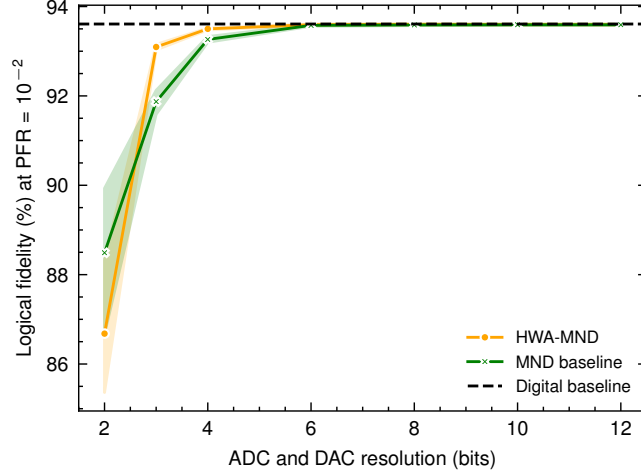


Figure S1. Impact of the analog-to-digital converter (ADC) and digital-to-analog converter (DAC) resolution on the recurrent neural network (RNN) decoder's test fidelity. The physical fault rate (PFR) is set to 10^{-2} . The test fidelity is obtained without including reading variability or defective devices, in order to assess the impact of resolution alone. At an 8-bit resolution, that is, 256 quantization steps between the boundary values -6 and 6 , the fidelity approaches the digital baseline fidelity (using a 32-bit floating point accuracy). The error range is obtained based on 10 independent training rounds.

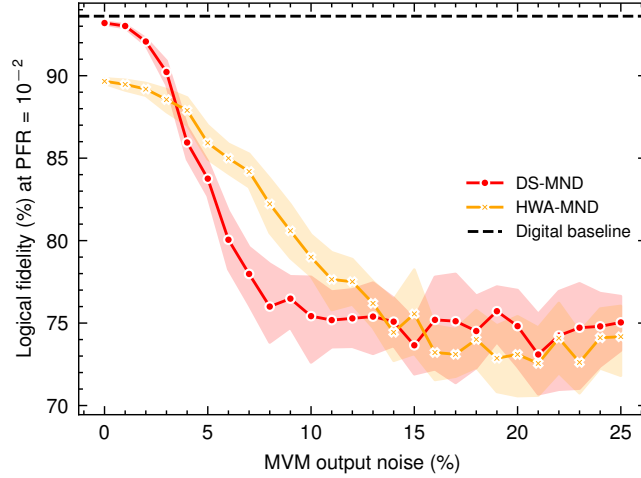


Figure S2. Impact of the matrix–vector multiplication (MVM) output noise on the recurrent neural network (RNN) decoder's test fidelity. The physical fault rate (PFR) is set to 10^{-2} . A random Gaussian value is added to the output of each memristor row to account for the expected reading noise produced by the electronic components and the memristors. The percentage is relative to the maximum logical output value (set to 6 in our simulations). All other non-idealities are kept as defined in Table S2.

require a re-training method addressing specifically this issue. However, it is worth noting that a dropconnect strategy, applied in addition to the DS-MND method, could mitigate the negative effect of reading variability.

S3. EXPERIMENTS ON TiO_x -BASED RESISTIVE MEMORY DEVICES

The studied TiO_x -based resistive memory devices are characterized by a Keysight Technologies B1500A semiconductor device parameter analyzer that has a 200 million samples/second waveform generator / fast measurement unit (WGFMU) using a Lake Shore CPX-VF probe station at room temperature. For all measurements, the electrodes at the bottom are grounded and the signals are applied to the electrodes at the top.

Conductance State Programming

In our study, the resistance of memristors is programmed using a closed-loop read–write–verify algorithm [34, 60]. This algorithm allows the programming of a memristor to a target resistance by applying successive read and write pulses. Initially, a device’s resistance is read using a read pulse (having a 0.2 V amplitude and a 1 μ s pulse width). If this measured resistance is larger than the target within a 1 % tolerance, a positive write pulse is applied (\sim 1 V amplitude and 200 ns pulse width); if it is lower, a negative pulse is applied. A read pulse is then applied to check the new resistance state, which starts a new cycle. The pulse amplitude is increased after each consecutive pulse of the same polarity by a constant step in order to converge to the target resistance. Using this read–write–verify algorithm for various target levels of resistance, we can perform multilevel programming as shown in Fig. 4(a) in the main manuscript.

Programming Variability Characterization

The programming variability model is based on experimental measurement conducted on TiO_x -based resistive memory devices. As shown in Fig. 4(a) in the main manuscript, multilevel programming is performed from the high-conductance states to the low-conductance states. To assess the cycle-to-cycle programming variability (shown in Fig. 4(b)), we successively perform multilevel programming from the low-conductance states to the high-conductance states 10 times. For each state and at each multilevel programming pass, the conductance is read 20 times and the mean value is kept. This process is repeated for 10 memristors to include device-to-device variability in the programming error model. The histogram of the mean programmed values for a conductance state is fitted by a Gaussian distribution and its standard deviation is extracted (also depicted in Fig. 4(b)). The fit of the standard deviation σ corresponds to the programming variability which depends on the conductance of the programmed state.

Conductance State Retention

The retention measurements presented in Fig. S3 are performed at room temperature for 8 hours for 5 conductance states. After the programming of a conductance state, a 1 ms-wide pulse with a 200 mV amplitude is applied every 5 minutes to measure the retention. The retention of the conductance states is measured successively. The 5 states demonstrate non-volatility over the eight-hour retention test. The conductance drift after 8 hours with respect to the initial conductance state can be fitted by a second-order polynomial function. Considering the small drift for this memristor technology, we have not considered this behaviour in the simulations presented in this paper.

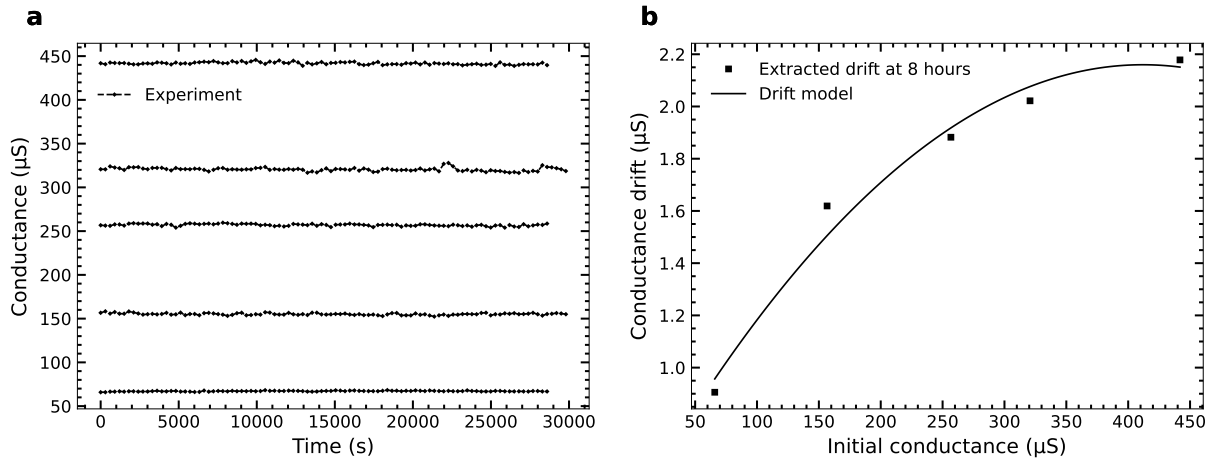


Figure S3. TiO_x -based resistive memory device retention study. (a) Retention of 5 conductance states between 65 μ S and 440 μ S. No conductance drift is noticeable. (b) Conductance drift of the 5 conductance states after eight-hour-retention measurements. The drift with respect to the initial conductance is fitted by a second-order polynomial function.

S4. NEURAL NETWORK TRAINING METHODS

Implementation of Training and Inference

The training of the RNN always begins with a classical deep learning [70] optimization process, using PyTorch [85] with no consideration for hardware non-idealities (see Fig. 5(a) in the main manuscript). The metaparameters used during this step are given in Table S1. In the case of hardware-aware memristive neural decoder (HWA-MND) and device-specific memristive neural decoder (DS-MND) re-training, the RNN parameters (weights and biases) are loaded from an earlier digital training, and one additional training epoch is run to adapt the model to newly introduced hardware constraints. Every other metaparameter remains unchanged during re-training.

Metaparameters	Values
Input size	4 rounds of 4 binary syndromes
Hidden layer size	32
Activation function	ReLU
Batch size	16
Loss	Cross-entropy
Optimizer	Adam [86]
Learning rate	0.001
Training epochs	4 (+1 for HWA and DS methods)

Table S1. Model and training metaparameters.

The RNN re-training and inference simulations are performed using the IBM Analog Hardware Acceleration Kit [69] v0.9.0. This Python library is used to simulate the computations executed on a crossbar array of memristors and the relevant peripheral circuit at the behavioural level. We extend the original toolkit to consider the specific TiO_x -based resistive memory devices used in our work. The non-idealities we discuss in the hardware characterization section of the main manuscript are implemented in the simulator. For instance, the statistical programming variability is calibrated on our TiO_x -based resistive memory devices.

Re-training methods

For hardware-aware re-training, the main manuscript focuses on introducing a dropconnect training method during the re-training of the MND to mitigate the effect of defective devices in the chip. However, there are other training methods that could improve performance. One such method consists in the addition of noise on weights during forward passes of training steps to account for the programming variability of the characterized TiO_x -based resistive memory devices. It has been shown that setting the training weight variability approximately equal to the inference weight variability is optimal [44]. However, in our case, we observed training instability issues with this method, which led to an unexpected gradient explosion in a fraction of the trained RNNs. Therefore, this method did not benefit the overall performance.

Hardware constraints and non-idealities	Simulated values
Weight clipping	2.5σ of the Gaussian distribution of each layer's weights' values
DAC resolution	8 bits
ADC resolution	8 bits
DAC max logical value	1
ADC max logical value	6
MVM output noise	Gaussian noise added with a standard deviation equal to 1 % of the maximum logical value (6)
Max memristor resistance	15 000 Ω
Min memristor resistance	5000 Ω
Memristor stuck-at-fault rate	10 %
Programming noise's polynomial fit	$y = -x^3(2.40 \times 10^{-5}) + x^2(1.15 \times 10^{-2}) - x(7.07 \times 10^{-2})$

Table S2. Default simulated values of the hardware constraints and non-idealities in our study. These values are used to simulate the memristor-based recurrent neural network (RNN) with the IBM Analog Hardware Acceleration Kit [69].

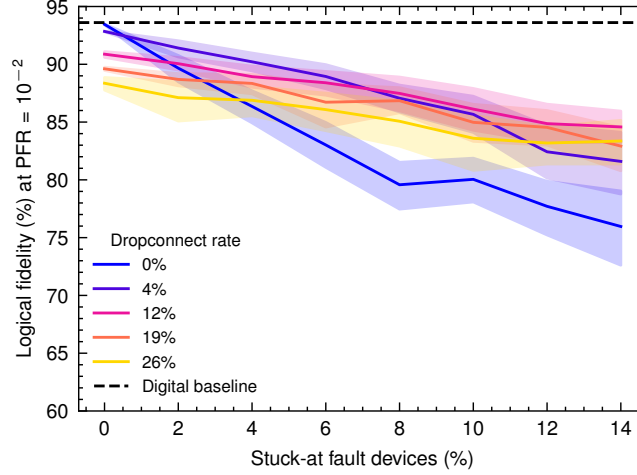


Figure S4. Impact of the dropconnect re-training method for various stuck-at-fault rates. Decoding fidelity at a physical fault rate (PFR) of 10^{-2} , for different dropconnect probabilities during hardware-aware (HWA) memristive neural decoder (MND) re-training, as a function of the percentage of stuck-at fault devices during inference. The shaded error regions represent the 95 % confidence interval over 10 random seeds.

The study of various non-idealities highlighted that only stuck-at fault devices have a critical effect on the performance of decoding. We attribute this to the fact that TiO_x -based resistive memory devices exhibit a low programming variability (in comparison to phase-change memory devices reported in [44]); therefore, injecting noise during training does not significantly improve fidelity. Also, an ADC and DAC of 8-bit resolution is sufficient for maintaining a fidelity close to the digital baseline, as explained in Supplementary Information Note S2. Thus, the input and output quantization during training does not allow for greater fidelity. Moreover, it is likely that the binary output of the model helps mitigate most noise-related issues since only a perturbation near the threshold value would impact the final binary output of RNNs.

Another limitation of memristors is their limited resistance range, which constrains the parameters' values. This limitation can easily be tackled to improve test accuracy by using a method called weight clipping to trim the parameters' values in a specific range during re-training [44]. It allows a certain degree of control over the weight distribution to make the programming of weights to hardware easier. It is performed by clipping the weights of a layer, after each backward pass in the training steps, within the range $[-\alpha\sigma; \alpha\sigma]$, where α represents the scale of the clipping, and σ is the standard deviation of the weight distribution of that layer. Based on our empirical tests, the exact value of σ does not appear to strongly affect the decoder's performance. Thus, we decided to fix $\sigma = 2.5$ for all MND test simulations.

The decoding fidelity globally improves when the dropconnect method is introduced during re-training compared to the case where no dropconnect is employed (shown using a blue curve with the label "0%" in Fig. S4). It also appears that an RNN decoder trained with a high dropconnect rate will have a lower fidelity if no device is stuck, but its performance will decrease more slowly when the rate of stuck-at fault devices increases. Therefore, a good trade-off between fidelity and robustness seems to be a dropconnect rate equal to the number of blocked parameters (19%) given the expected stuck-at fault device percentage (10%). Since a parameter is encoded by two devices (for positive and negative values), the probability of a parameter being blocked (i.e., set to 0%) is equal to the probability of at least one of the pair of devices being stuck.